Purified and Crystalline Three-Dimensional Electron-Beam-Induced Deposits: The Successful Case of Cobalt for High Performance Magnetic Nanowires

Javier Pablo-Navarro[1], César Magén[1,2,3,4] and José María de Teresa[1,2,3]*

[1] Laboratorio de Microscopías Avanzadas (LMA) - Instituto de Nanociencia de Aragón (INA), Universidad de Zaragoza, 50018 Zaragoza, Spain.

[2] Instituto de Ciencia de Materiales de Aragón (ICMA), Universidad de Zaragoza-CSIC, 50009 Zaragoza, Spain.

[3] Departamento de Física de la Materia Condensada, Universidad de Zaragoza, 50009 Zaragoza, Spain.

[4] Fundación ARAID, 50018 Zaragoza, Spain.

KEYWORDS. magnetic nanowires, focused electron beam induced deposition, cobalt, annealing, transmission electron microscopy, electron holography

ABSTRACT. Focused electron beam induced deposition (FEBID) is considered the ultimate direct-write lithography technique for three-dimensional (3D) structures. However, it has not been possible yet to obtain 3D deposits by FEBID with the same purity and crystallinity of the corresponding bulk materials. In the present work, purified and crystalline 3D cobalt nanowires of diameter below 90 nm have been fabricated by ex-situ high-vacuum annealing at 600 ºC after FEBID growth. While increasing the metallic content of the nanowires up to 95% at., the thermal annealing process induces the recrystallization of the pseudo-amorphous as-grown structure into bulk-like, *hcp* and *fcc* crystallites with lateral sizes comparable to the nanowire's width. The net magnetization increases 80% with respect to as-grown values, up to 1.61 ± 0.06 T, near bulk cobalt. This achievement opens new pathways for applications of this synthetic method in the fabrication of either individual or arrays of 3D high-purity and crystalline cobalt nanowires for high-density memory and logic devices, nanosensors and actuators, and could be a viable method to obtain other pure and crystalline 3D materials by FEBID.

Focused electron beam induced deposition (FEBID) is a synthetic technique, competitive for the fabrication of nanoscale objects and devices in a single-step lithographic method, not requiring the use of masks or lift-off procedures to fabricate motifs of nearly arbitrary shape and dimensions in a great variety of substrates[1–3]. The versatility of this direct-write nanofabrication technique to grow metallic[4], insulating[5], ferromagnetic[6,7] or superconducting[8] materials, combined with its capability for three-dimensional growth[9], has stimulated the search for applications in fields as diverse as nanocontacting[10], circuit edit and mask repair[11], plasmonics[12,13], photodetection[14], magnetic storage and logics[15,16], gas[17] and magnetic sensing[18], nano-actuation[19], etc. FEBID implies the electron-beam-induced decomposition of a metal-organic gas precursor adsorbed on the growth surface, fundamentally driven by the secondary electrons emitted by the substrate or the nascent deposit material[3]. The metal deposits generally contain different levels of contaminants originating from partially-decomposed precursor molecules and from dissociation of residual gases in the growth chamber[20]. Even though the smart tuning of the growth parameters (primary beam voltage and current, base pressure, precursor flux, dwell time, etc.) enables the growth of relatively-highly-metallic deposits[18,21–24], in many cases the as-grown metallic content is remarkably low. For example, Pt deposits grown by FEBID with the standard precursor $(CH_3)_3Pt(CpCH_3)$ only contain 18% of Pt, in the form of 3 nm small grains, the rest being C and O[25]. Thus, the lack of purity and the poor crystallinity will in general be limiting factors for obtaining the full potential of FEBID.

Diverse approaches have been followed to increase the purity of FEBID deposits, as reviewed by Botman et al. in 2009[20], and further explored since. This includes the growth on substrates at elevated temperatures[26–28], in-situ annealing in high vacuum[29–31], electron beam irradiation[32,33], exposure to reactive atmospheres[34,35], laser-assisted heating during deposition[36,37], post-growth Joule heating upon injection of high electric

currents[38], ex-situ annealing[39,40], supersonic jet delivery of precursor gas[41], and combinations of all these methods[35,42–46]. Astounding success has been achieved in growing virtually-pure Pt deposits by post-growth electron irradiation in oxygen atmosphere[34], or functional Au plasmonic nanostructures by electron beam irradiation in water vapor atmosphere[13]. However, such strategies have been generally applied to 2D deposits and challenges remain for their application to 3D deposits, such as the high volume shrinkage occurring due to the low metal content in the original deposit, which leads to substantial modification of the deposit shape or even the collapse of the 3D structures.

The case of magnetic materials grown by FEBID merits a separate discussion. Cobalt and iron deposits are amongst the FEBID materials with highest metallic content levels[47–49]. In this case, purity and crystallinity will have great impact in their electrical transport[31] and magnetic properties (saturation magnetization, magneto-crystalline anisotropy, coercive field, etc.)[50,51], both key for the potential application of FEBID magnetic deposits. 2D Co deposits are mostly based on the metal-organic precursor dicobalt octacarbonyl, $Co_2(CO)_8$. As-grown high metal contents up to 95% at. Co with metallic behavior upon optimum growth conditions have been achieved with limited lateral resolution and small crystalline size[47]. Even so, C and O contamination is always present due to the incomplete decomposition of the precursor molecules or residual chamber contaminants. 2D Fe deposits can be grown with high purity and small crystal size in ultra-high vacuum environment, which is a too-demanding condition for many applications[22]. In the case of 3D magnetic deposits, the dispersion of composition values found in the literature is high, given the strong dependence of the growth mode to small changes in the numerous growth parameters[48,50]. To the best of our knowledge, the growth of pure and fully-crystalline 3D magnetic deposits by FEBID has not been reported so far

and is likely not possible without post-processing. The first attempts to purify Fe deposits were carried out by Furuya et al. through ex-situ thermal annealing and electron beam irradiation in ultra-high vacuum, demonstrating the formation of highly-magnetic alpha-iron deposits, in some cases coexisting with iron carbides[39]. 3D nanostructures were already subjected to post annealing up to 600 ºC achieving iron contents near 60% at. Fe.[30] Studies on FEBID Co include the work by Belova et al., who analyzed carbon-seeded micrometric deposits grown on substrates at 70 ºC, on the verge of the thermal decomposition of the precursor, which presented a metal content >95% at. Co.[27] Begun et al. explored the catalytic activity of Co in a reactive atmosphere (H_2) upon electron beam irradiation, observing the formation of metallic Co only in a 20-nm-thick surface region of the deposit[44]. The effect of intense electric current on the properties of suspended Co nanowires has also been reported to induce purification from 80% to 89% at. Co and crystallization into large *fcc* crystals caused by local Joule heating and electromigration[38]. Recently, post-growth annealing in high vacuum of thin Co stripes increased its composition from 67% to 84% at. Co, with a conductivity of metallic character and three orders of magnitude higher than as-grown[31]. Although such previous work has provided hints on how to improve the purity and crystallinity of magnetic deposits grown by FEBID, the procedure to obtain purified and crystalline 3D magnetic deposits maintaining the original shape has not been reported yet. Hereafter, such successful post-processing method will be described for 3D cobalt nanowires. Given its simplicity, it will facilitate the development of future applications based on 3D magnetic nanostructures.

In the present work, we draw our attention to the synthesis of pure and fully-crystalline cobalt nanowires of lateral size below 90 nm by FEBID growth and subsequent ex-situ annealing at temperatures up to 600 ºC in high-vacuum conditions. These

nanowires present 70% at. Co after FEBID growth, increasing to 95% at. Co after post-processing. The saturation magnetization reaches the value of 1.61 ± 0.06 T after post-processing. Moreover, volume shrinkage after post-processing is not observed, ensuring good mechanical stability of the 3D structures during the process, in sharp contrast to other FEBID 3D materials with low metal content in the as-grown material. These results demonstrate that optimizing growth conditions to maximize cobalt content of as-grown nanostructures is not a key requirement provided that it is 65% at. or higher. To the contrary, the attention of as-grown FEBID magnetic nanostructures can be focused on tailoring the lateral dimensions and increasing architectural accuracy and complexity to produce individual or arrays of customized 3D nanostructures, which can be later annealed ex-situ to obtain devices of pure material with optimum magnetic response for the numerous applications foreseen for these structures, i.e. magnetic data storage and logic systems, Hall-effect nanosensing, catalytic growth of nanostructures, cantilever functionalization, or magnetic nanoactuators[49].

RESULTS AND DISCUSSION

The fabrication of as-grown 3D Co nanowires by FEBID is performed with the optimal growth parameters reported in previous works to obtain small diameter nanostructures (around 90 nm) with high aspect ratio (>15) and moderately high Co composition, >65% at. Co (see Methods)[50]. With these conditions, a net magnetic induction of 0.80 ± 0.05 T is obtained by the combined effect of low purity and surface oxidation. Energy dispersive X-ray spectroscopy (EDS) chemical analysis performed at half height of nanowires length, approximately where the magnetic characterization by electron holography is later performed, showed that the composition of the nanowires was 65 ± 3 % at. Co, 23 ± 3 % at. C and 11 ± 1 % at. O. No significant changes in the chemical composition have been observed along the nanowire, except near the base, where oxygen signal from the copper

grid is also collected.

Five sets of specimens have been grown right on five Cu grids for transmission electron microscopy (TEM), labelled from A to E. The post-growth annealing processes were carried out for 100 minutes in grids B-E at different temperatures; 150 ºC (sample B), 300 ºC (sample C), 450 ºC (sample D) and 600 ºC (sample E), keeping sample A as the reference as-deposited sample at 24 ºC. Each of the rest has been annealed. Table 1 summarizes the annealing condition of each of these samples. All the nanowires are exposed to air before and after the annealing procedure, suffering surface oxidation.

Table 1. Annealing conditions of each of the FEBID cobalt nanowires studied.

Sample	Annealing temperature (ºC)	Annealing time (minutes)	Start pressure (10^{-6} mbar)	Final pressure (10^{-6} mbar)
A	-	-	-	-
B	150	100	2.3	3.6
C	300	100	2.5	3.4
D	450	100	3.2	4.5
E	600	100	4.0	7.4

High resolution transmission electron microscopy (HRTEM) imaging and chemical mapping by electron energy loss spectroscopy (EELS) in scanning transmission electron microscopy (STEM) mode have been used to track the structural and chemical evolution of the nanowires upon increasing annealing temperatures. Firstly, the as-grown nanowires (see Figure 1a) display the expected nanocrystalline microstructure, with no texture. The Fast Fourier Transform (FFT) of a 12 x 12 nm^2 region of the image reveals just a diffuse diffraction ring. Also, the presence of a ~5 nm-thick layer of Co_xO_y covering the whole nanostructure can be detected in the HRTEM image, as a brighter, lower density thin layer at the surface.[52] The EELS chemical map also depicts an oxygen-rich layer of comparable size surrounding the nanowire (see Figure 2a). Interestingly, the oxygen content inside

the nanowires is not perfectly homogeneous, but gradually increases from the core towards the surface. In a previous work[53], we evidenced that the surface oxidation layer is not ferromagnetic, causing an overall deterioration of the ferromagnetic properties. The negative impact of the surface oxidation can be palliated by growing a protective shell to increase the overall net magnetization by ~17%, still rather far from bulk cobalt.[53] However, the use of protective layers has been discarded in the current work in order to separate clearly the impact of annealing on the properties of the cobalt nanowires. The evolution of the nanowires' microstructure and chemical composition upon increasing annealing temperature is illustrated in Figure 1(b-e) and Figure 2(b-e). The crystallinity increases as the annealing temperature rises. Grain size is hard to quantify accurately due to the density and superposition of the crystals, but it can be roughly estimated by inspecting the HRTEM images and the features of the FFT. At 150 ºC some individual spots can be also identified, see Figure 1(b), in the digital diffractogram of the nanowire together with the diffuse diffraction ring, denoting the presence of grains of larger size, with sufficient crystalline coherence to produce clear Bragg diffraction spots. Diffusion of contaminants has already begun, as the oxygen distribution turns out to be more inhomogeneous. At 300 ºC diffuse scattering has disappeared in the FFT and large cobalt grains have grown to reach diameters around 10-15 nm. Well-defined oxygen-rich regions have clearly segregated all over a higher purity cobalt matrix, which correspond to cobalt oxide nanoparticles with a typical size of around 10 nm, estimated from EELS chemical maps. Among the most common cobalt oxides, CoO is stable up to 900 ºC in air and ambient temperatures, while it tends transforms into Co_3O_4 around 600-700 ºC,[54] much above the annealing temperatures discussed in this work. Thus, even though the stoichiometry cannot be determined, it is plausible that the observed oxide particles are CoO. Nanowires annealed at 450 ºC present abundant regions where the FFT evidences a single crystalline pattern. This indicates that, in these areas, the grain size is large

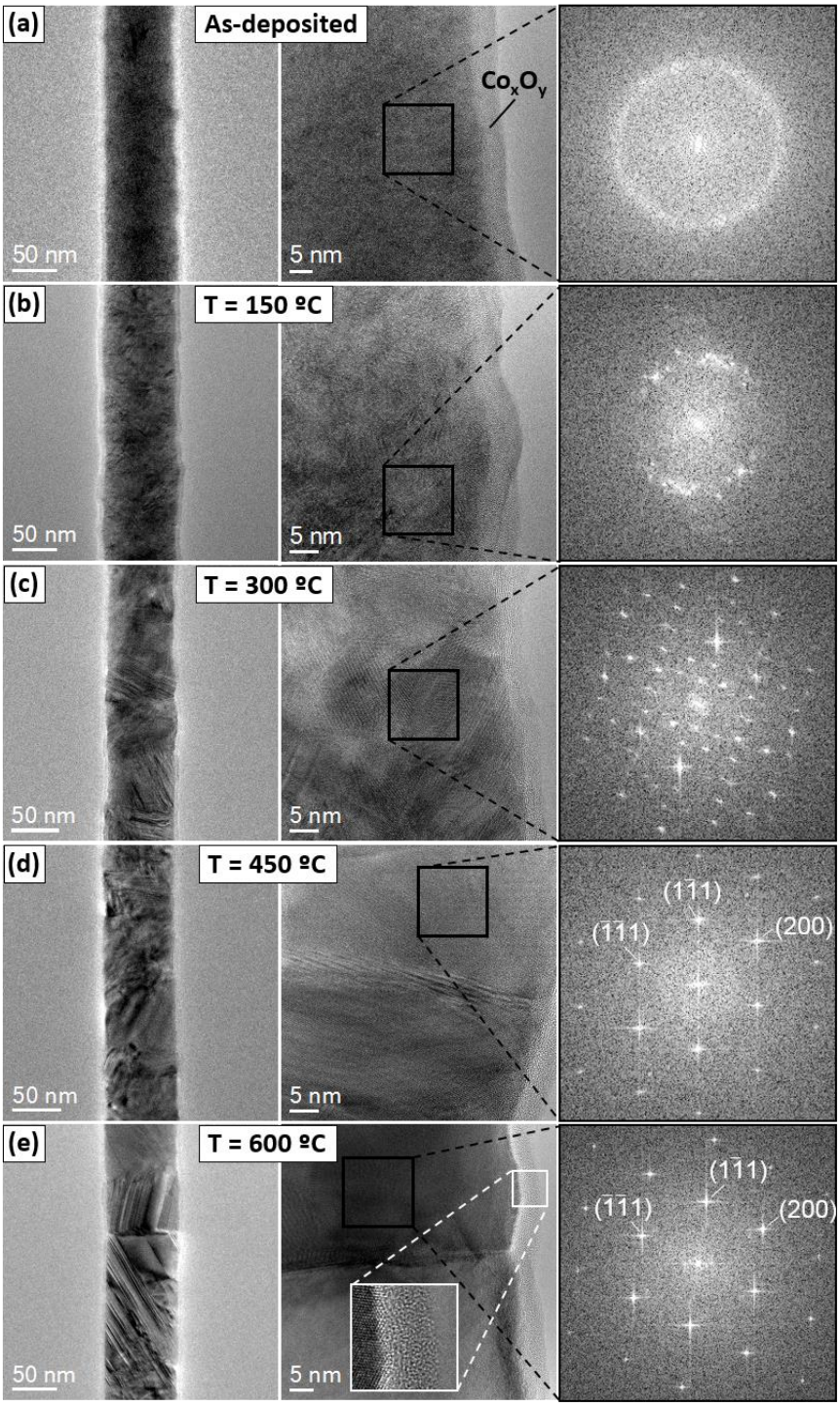

Figure 1. TEM (left column) and HRTEM (central column) images of (a) an as-deposited Co-FEBID and the ones annealed at (b) 150 ºC, (c) 300 ºC, (d) 450 ºC and (e) 600 ºC. Each sample case is accompanied by the corresponding Fast Fourier Transform (FFT) of a 12 x 12 nm^2 area of the image (right column). Indexed FFT images correspond to *fcc* (011).

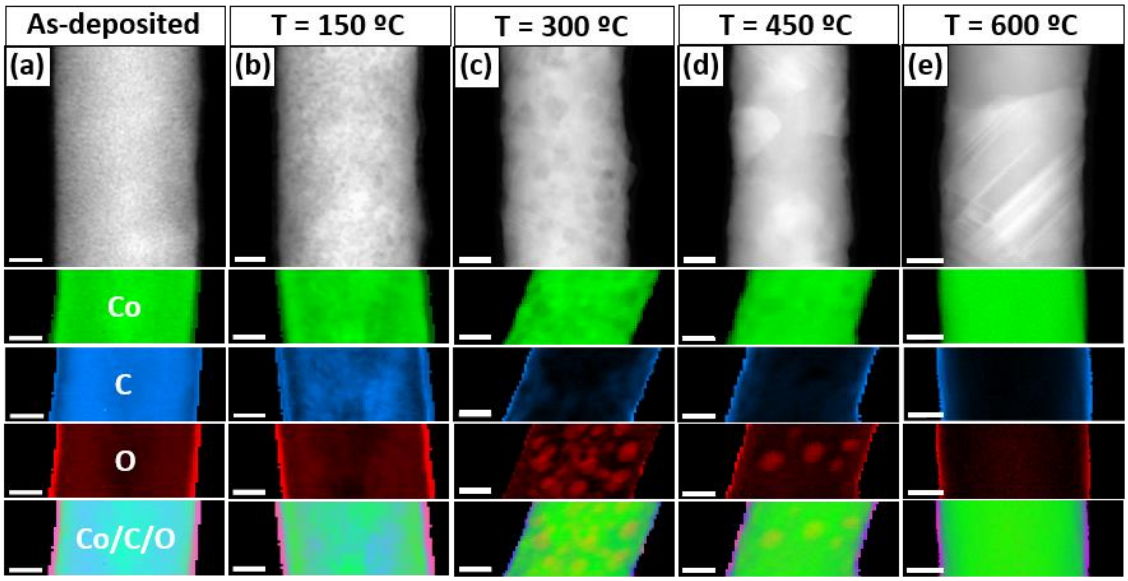

Figure 2. HAADF-STEM images (first row) and STEM-EELS chemical maps of (a) an as-deposited Co-FEBID nanowire and the ones annealed at (b) 150 ºC, (c) 300 ºC, (d) 450 ºC and (e) 600 ºC. The chemical maps show the spatial distribution of Co, C and O, in green, blue and red, respectively. The lowest panels represent relative compositions of Co, C and O in the same images. The undefined scale bars are 20 nm in all images.

enough to not overlap with other crystals. When they do, mostly in the boundaries between two large crystals, Moiré fringes may appear in the STEM and HRTEM images. In turn, this means that the grain size is becoming comparable to the diameter of the nanowire. Additionally, this causes the drastic diminution of the number of oxygen-rich grains with respect to annealing at 300 ºC. In the end, the annealing at the highest temperature of 600 ºC gives rise to a nanowire composed by a succession of large single-crystals as wide as the nanowire itself. Remarkably, a grain boundary spanning the whole nanowire width and separating two large crystals is observed, as shown in Figure 1(e). Cobalt crystals presenting *hcp* and *fcc* structure have been found. Microstructure of the nanowires as a function of the annealing temperature is further illustrated in Figure S2 and S3 of the Supporting Information (SI), where selected area diffraction patterns,

HRTEM images of representative grains of both structures and their respective FFTs are shown for different annealing temperatures. At 600 ºC chemical maps in Figure 2(e) evidence that oxygen has practically disappeared inside the nanowires, whilst the natural oxidation still remains at the surface.

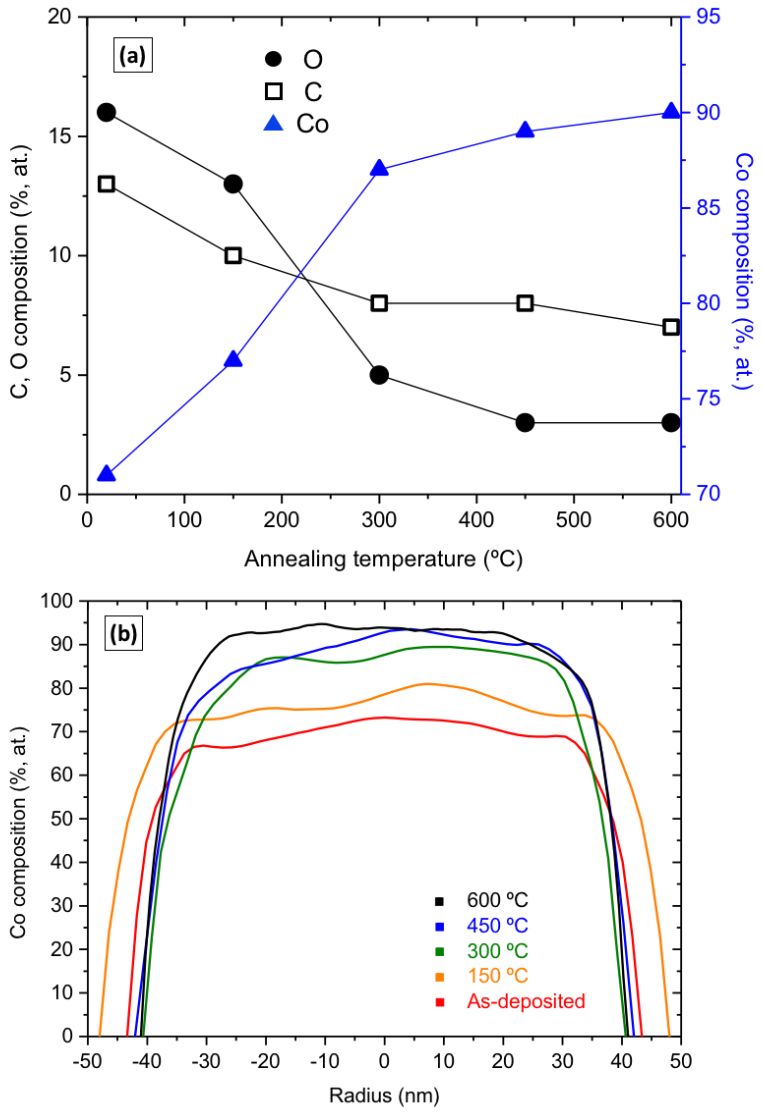

Figure 3. (a) Overall composition of the Co-FEBID nanowires as a function of the annealing temperature extracted from the integration of Co, O and C signals of the STEM-EELS spectrum images in Figure 2. (b) Profiles of the Co composition of the Co-FEBID NWs as a function of the radial position for different annealing temperatures.

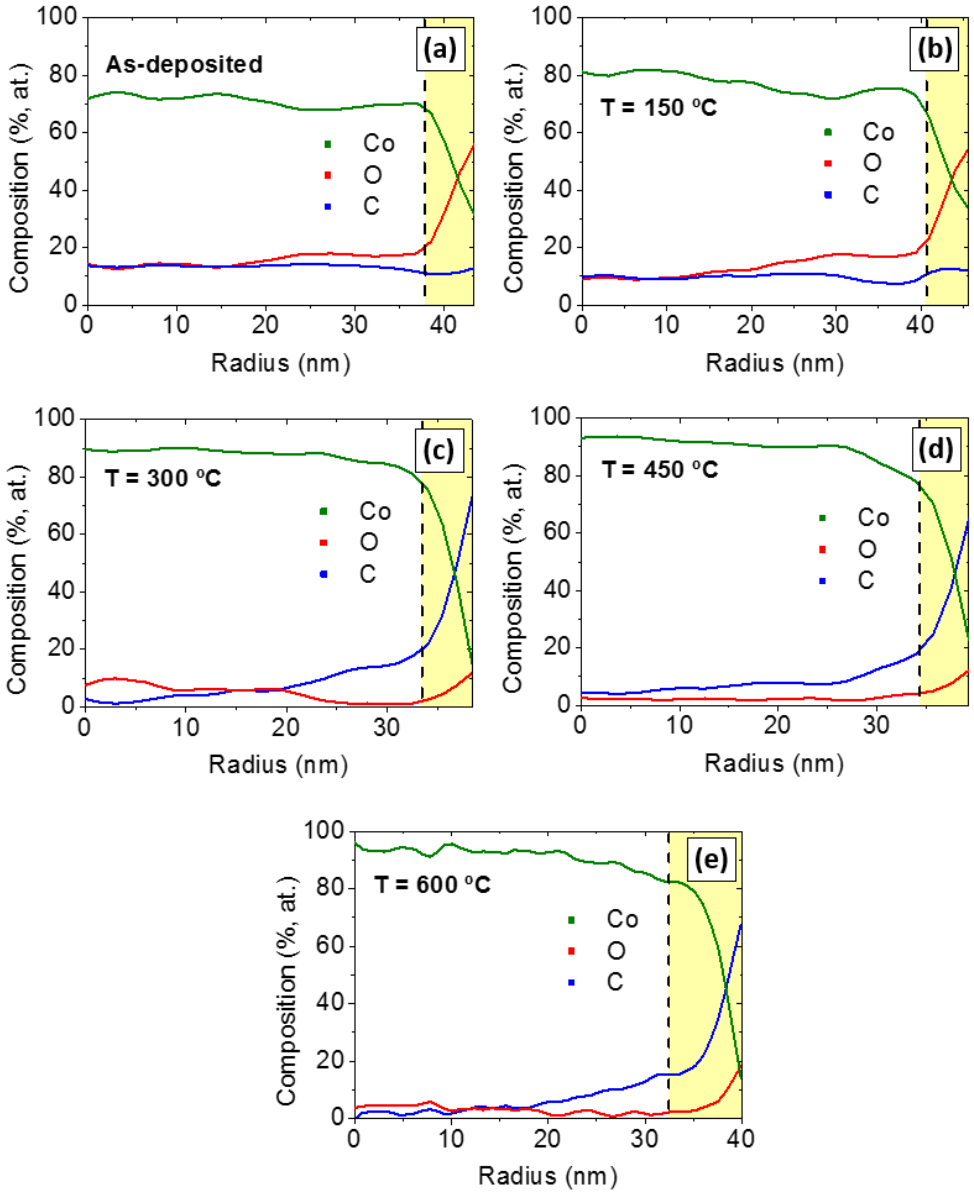

Figure 4. STEM-EELS profiles of the Co (in green), O (in red) and C (in blue) compositions as a function of the radius of (a) an as-deposited Co-FEBID nanowire and the ones annealed at (b) 150 ºC, (c) 300 ºC, (d) 450 ºC and (e) 600 ºC. Yellow bands and dashed lines are guides to the eye showing the shells of the nanostructures.

A key aspect for technological application of this annealing process is preserving the original architecture of the nanostructure. As illustrated in Figure S1 of the SI, the diameter and length of the Co-FEBID nanowires are virtually the same before and after the annealing treatment, even at the highest annealing temperature of 600 ºC. As no

significant reduction of the volume occurs, the shape of the as-grown nanostructure is conserved, enabling the application of this method to complex architectures.

A more quantitative analysis of the composition of the Co-FEBID nanowires as a function of the annealing temperature is shown in Figure 3. The overall Co composition of the nanowires, obtained from the integration of the spectrum images shown in Figure 2, is plotted in Figure 3(a). The average metallic content increases from approximately 70% at. Co of as-deposited nanowires up to 90% at. Co after annealing at 600 ºC. Both carbon and oxygen content decrease showing different dependences. While the oxygen diminishes from 16% at. O (as grown) to 3% at. O (600ºC annealing), carbon content decreases more slowly from 13% to 7% at. C. This means that while oxygen virtually disappears from the structure (except the possible oxidation of the surface), about 50% of the original carbon contamination remains after annealing at the maximum temperature. Figure 3(b) shows the radial dependence of the Co composition as a function of the annealing. The metallic content increases from 70% at. Co in the as-grown sample up to 95% at. Co at 450 ºC and above. This evidences that, except for the outer surface of the nanowire where natural oxidation and accumulation of non-volatile contaminants migrate, the inner part of the nanowire is virtually pure. Local variations of Co composition at intermediate temperatures are related to the presence of oxide grains observed in the EELS maps. Interestingly, the composition of the non-ferromagnetic nanowire surface also changes with temperature annealing, as shown in Figure 4. For the as-grown and 150 ºC-annealed nanowires the O/C ratio is over 1. However, for those NWs annealed at 300 ºC or higher temperatures, the O/C ratio is reversed, particularly in the surface where the carbon content increases dramatically up to 60-70% at. C. The spatially resolved quantification of the chemical composition of the annealed nanowires shown in Figures 3 and 4 gives some clues about the annealing process. Puydinger et al.

reported that the expected mechanism for purification of Co-FEBID deposits is the thermal activation of precursor residues in the form of CO or CO_2.[31] Upon thermal annealing these volatile species migrate to the surface and evaporate, which accounts for the practically complete loss of oxygen except for the inevitable surface oxidation. The remaining carbon is non-volatile and accumulates in the surface at high annealing temperatures, in agreement with the observation of partially graphitized carbon at the surface of the nanowires even after annealing at 600 ºC, see Figure 1(e). In these conditions the nanowires are apparently more resistant to oxidation, as the surface oxygen content after annealing is much diminished with respect to as-grown nanowires. Indeed, the formation of a ~5-10 nm carbonaceous layer may act as a protective coating from oxidation.

The drastic increase of cobalt content upon annealing must have a direct consequence on the magnetization of the nanowire. The remanent net magnetic induction along the nanowire's axis (B_x), averaged across the thickness of the sample along the electrons trajectory, has been estimated by electron holography (see Methods). As shown in Figure 5, the purification of the Co nanowires upon thermal annealing also strengthens the magnetization. Magnetic induction sharply increases in the first stage of annealing, from 0.80 ± 0.05 T as grown up to 1.09 ± 0.05 T at 150 ºC, 1.20 ± 0.05 T at 300 ºC and around 1.32 ± 0.05 T at 450 ºC, tending to stabilize at this value up to the highest annealing temperature at 600 ºC with 1.36 ± 0.05 T. This enhancement of the net magnetization as a function of the annealing temperature replicates the rise on metallic content, both increasing gradually until they tend to saturate around 450 ºC. It is worth noting that the presence of large *hcp* and *fcc* crystals, which implies the appearance of significant magneto-crystalline anisotropy,[55] does not affect the remanent orientation of the magnetization of the nanowires. This is evidenced by the perfectly axial orientation

of the flux lines all along the regions of the nanowires studied. Therefore, the strong magnetic shape anisotropy of high aspect ratio Co nanowires still dominates.

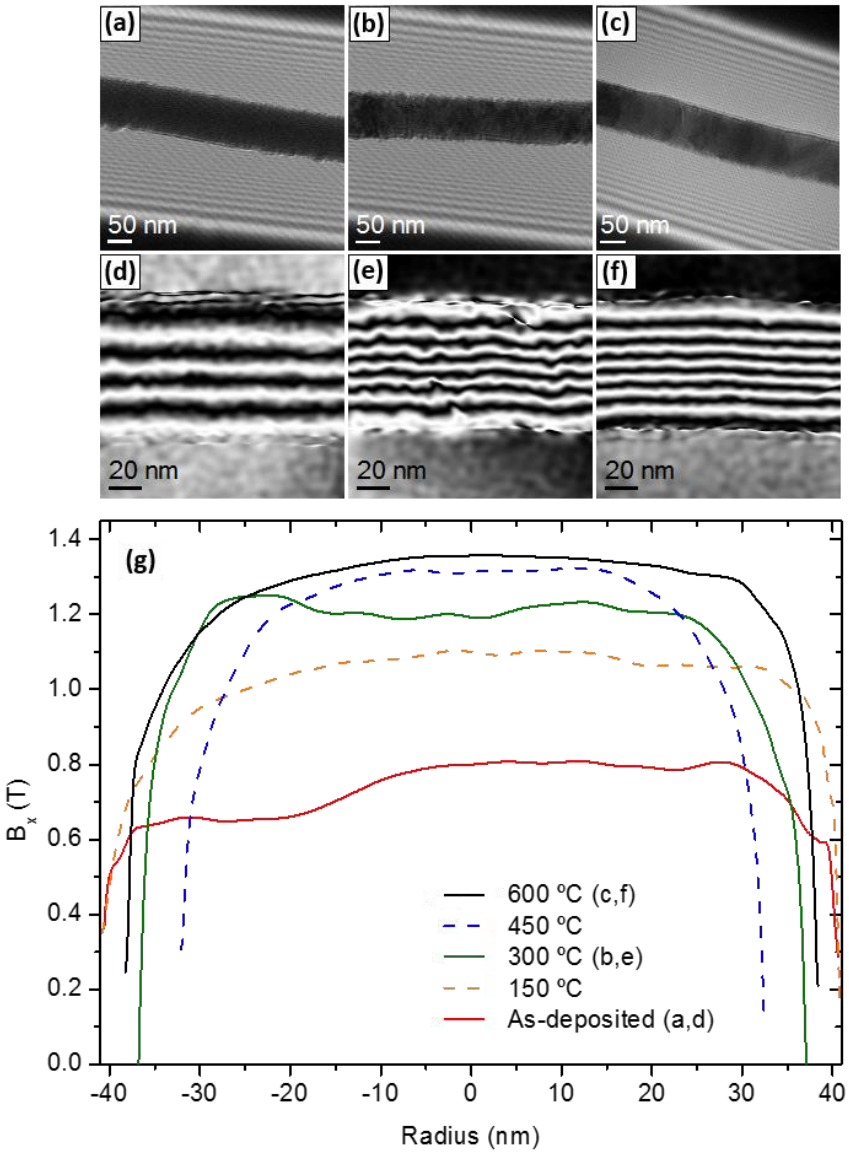

Figure 5. Electron holograms and magnetic induction flux representations of 3D Co-FEBID nanowires (a,d) as-deposited, (b,e) annealed at 300 ºC, and (c,f) annealed at 600 ºC. The magnetic induction flux images are obtained by normalizing the magnetic phase ones to the diameter (maximum thickness) and calculating the cosine of 350 times the normalized magnetic phase. (g) Profile of the thickness-averaged axial component of magnetic induction (B_x) calculated for the Co-FEBID nanowires as a function of the

annealing temperature.

The chemical quantification and the novel microstructure observed after high-temperature annealing indicates that the inner part of the nanowires is virtually pure cobalt. However, the estimated magnetic induction of 1.36 T is still far from the bulk value of 1.76 T. One reason for this discrepancy is the fact that carbon migration to the nanowire's surface plus the possible oxidation of the outer part of the nanowire make that the effective magnetic thickness of the nanowire is less than the nominal one. Therefore, the structural model would be that of a pure cobalt nanowire covered at the surface by a 5-10 nm thick layer of non-magnetic shell composed of diffused residual carbon contaminants and naturally-oxidized cobalt formed upon exposure to air. If the shell thickness is neglected from the calculation just taking into account the core diameter (estimating an approximate average contamination shell thickness of 7.5 nm for the highest annealing temperature), the magnetic induction increases up to 1.61 ± 0.06 T, much nearer to bulk cobalt values already found in 2D deposits.[18] In fact, a similar correction on the chemical composition would bring the metallic content of the inner part of the nanowire closer to 100% at. Co. The estimated magnetic induction values, corrected by the thickness of the non-magnetic shell, have been plotted in comparison with the cobalt content as a function of the annealing temperature in Figure 6. The correlation between these magnitudes is clear and follows the same trend, i.e. both increase gradually up to 300 ºC annealing, then tend to saturation at 450 ºC.

The successful application of post-growth purification procedures to FEBID cobalt presents a new scenario in which, instead of maximizing metallic content during deposition, the optimization of growth conditions can be focused on other key parameters such as lateral size, geometric complexity or growth rate,[15,46] which are key for the implementation of 3D FEBID deposits as racetrack memories, magnetic sensors or

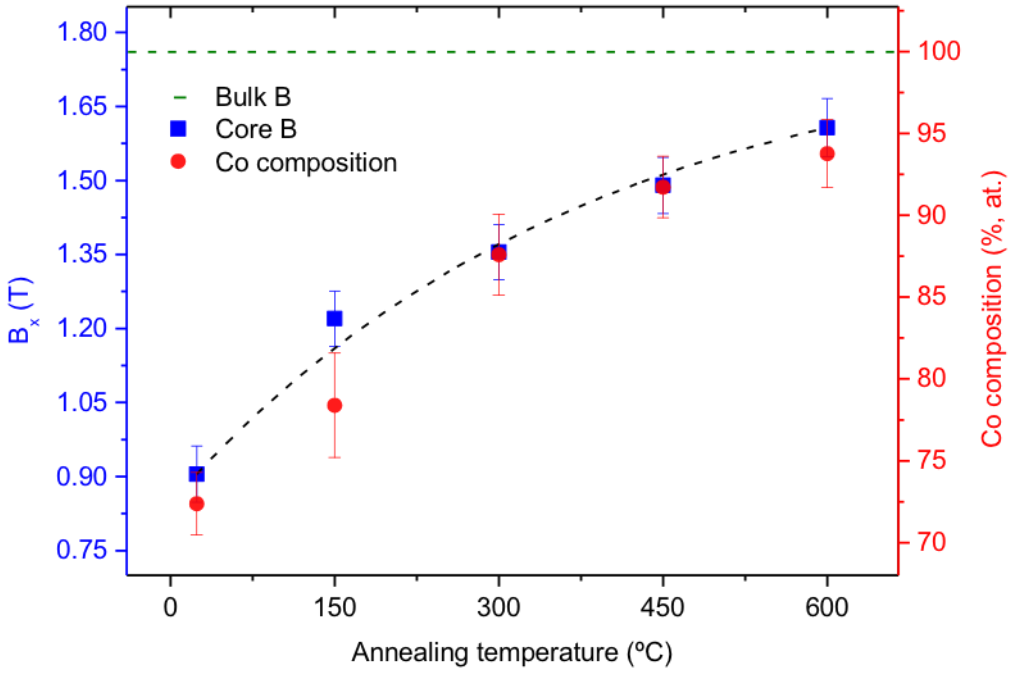

Figure 6. Average net magnetic induction and Co composition as a function of the annealing temperature considering the experimental data extracted from the central 20 nm of each nanowire.

actuators. In this line of thought, future progress in the purification of FEBID cobalt nanowires could point towards exploring further crystallization upon longer annealing times with the aim of producing single crystalline nanowires, the use of reactive atmosphere to etch the remaining contaminants at the surface,[44] or annealing of core-shell nanowires in which a novel metal coating (Pt, Au) protects the magnetic core from air exposure.[52] In this sense, the application of this procedure to other FEBID materials should be analyzed carefully. Our approach does not suggest that as-grown metallic content is not an issue anymore. To the contrary, it is reasonable to think that the as-grown metallic content must reach a certain level in order to prevent a remarkable volume shrinkage and eventually the destruction of the device during annealing. In the case of cobalt, we demonstrate that 65% at. Co is sufficient to guarantee the architectural stability

of the initial design. However, in the example of low-purity Pt-FEBID discussed in the introduction, which corresponds to small Pt nanoparticles in a carbonaceous matrix, it is likely that a similar process[25] causes a large volume reduction and the collapse of the structure. Thus, further progress in the growth of as-grown deposits with higher metallic content would be required before applying the method described here.

CONCLUSIONS

In summary, post-growth ex-situ annealing in high-vacuum of 3D cobalt nanowires grown by FEBID has been performed. Our results demonstrate that thermal annealing at 600 ºC produces purified and crystalline cobalt nanowires with a diameter below 90 nm, a metallic content above 95% at. Co, and a net magnetization up to 1.6 T. The combined effect of contaminants migration to the surface and recrystallization of as-grown nanocrystalline structure gives rise to narrow 3D nanowires with physical properties close to bulk cobalt. Given the relatively high metal content of the as-grown deposits, the change in shape of the deposit after purification is minimal, facilitating their functional implementation in 3D devices. The results shown are a forward step towards the ultimate goal of driving FEBID towards a practical lithography technique to fabricate 3D functional nanostructures with unique lateral resolution.

METHODS

Growth of the 3D Co nanowires by FEBID. The nanostructures were grown in the commercial Helios Nanolab 650 Dual Beam system equipped with a Schottky field emission gun (S-FEG) electron column and a gas injector system (GIS) for depositing Co using $Co_2(CO)_8$ precursor gas. After the optimization of the parameters, the deposits were fabricated in TEM Cu grids selecting an electron beam voltage of 5 kV, an electron beam current of 100 pA and a chamber growth pressure of 2.6×10^{-6} mbar. To reduce the

contamination of the deposit due to residual gases, the deposition chamber was evacuated until a base pressure of 1.3×10^{-6} mbar was reached. The growth pattern was a single patterning point scanned by the electron beam 1.7×10^{7} times during 45 second. The scanning of it gives rise to a vertical segment which constitute the 3D nanowire.[50]

Compositional analysis by energy dispersive X-ray spectroscopy. Energy dispersive X-ray spectroscopy (EDS) experiments were carried out in the Helios Nanolab 650 Dual Beam system with the APOLLO X detector using the EDAX software. Semi-quantitative standardless EDS chemical analysis has been carried out. Only Co, C and O elements are considered to give the atomic content (in atomic percentage). The experiments were performed before the annealing process and after the natural oxidation of the nanowires, using an electron beam voltage of 5 kV, an electron beam current of 800 pA, and a base pressure of 1.43×10^{-6} mbar.

Ex-situ post-growth annealing experiments. The post-growth ex-situ annealing took place in an SEM Quanta FEG 250 system equipped with a heating stage in high vacuum. To minimize contamination during annealing, the SEM chamber was initially evacuated until the base pressure decreased below 4×10^{-6} mbar. A heating ramp of 50 ºC/min was programmed, which corresponds to the maximum allowed by the equipment, until the target annealing temperature for each sample was reached. Then the samples were annealed at 150 ºC, 300 ºC, 450 ºC and 600 ºC for 100 minutes. The base pressure increased during the early stages of the annealing process due to degassing of the SEM components near heating stage before falling back to a lower level until the experiment finished (see Table 1). After annealing, the heater was switch off and the specimen was cooled down freely to room temperature. Longer annealing times were tested (for instance, 500 min at 600 ºC). The resulting nanowires did not conserve the original architecture and pure cobalt sections (see Figure S4) were intermixed with carbonaceous

ones, so no further tests were made.

Microstructural and compositional analysis by transmission electron microscopy. High resolution transmission electron microscopy (HRTEM) imaging was performed in a Titan Cube 60-300 operated at 300 kV and fitted with an S-FEG, a CERCOR aberration corrector for objective lens from CEOS providing sub-angstrom point resolution, and a 2K × 2K Ultrascan CCD camera from Gatan. Selected area electron diffraction was carried out in a Tecnai T20. Scanning transmission electron microscopy (STEM) and electron energy loss spectroscopy (EELS) experiments were carried out in Titan Low Base 60-300 system operated at 300 kV. This microscope is equipped with a high brightness field emission gun (X-FEG), a CETCOR corrector for the condenser system which produces an electron probe with a lateral size below 1 Å. The STEM-EELS experiments were performed using a Gatan Image Filter (GIF) Tridiem 866 ERS, with a 25 mrad convergence semi-angle, an energy dispersion of 0.5 eV/pixel with a resolution of 1.5 eV, a GIF aperture of 2.5 mm, a camera length of 10 mm, a pixel time of 15 ms and an estimated beam current of 270 pA. Examples of the EELS spectra collected are illustrated in Figure S5.

Determination of the magnetic induction (B) of nanowires by off-axis electron holography. Off-axis electron holography experiments were performed in the Titan Cube 60-300 described previously. This instrument is also equipped with a motorized electrostatic biprism placed at the selected area apertures holder and a Lorentz lens located below the objective lens to enable magnetic-field-free imaging. The experiments were realized at 300 kV by switching off the objective lens and using the Lorentz lens as the image-forming lens. The biprism was excited at 150 - 170 V to create the overlapping area of ranging from 400 nm to 500 nm width, with a fringe contrast ranging from 20% to 25%. The hologram acquisition time was 5 s. The holograms were acquired in

remanence state after the saturation of the magnetization in the two opposite directions along the longitudinal NW growth axis, so the electrostatic phase shift (which conserves its sign upon magnetization reversal) caused by the mean inner potential can be easily discounted and the magnetic phase shift (φ_{MAG}) extracted. Saturation was achieved by tilting the nanowires' axes by 30º and exciting the objective lens up to 10% excitation, which corresponds to an axial magnetic field of 0.3 T. Central regions of the nanowires were analysed, far from the tip where the presence of stray fields makes that magnetic induction is not perfectly along the nanowire's axis (see Figure S8). If the nanowire axis is set along the *x* axis, the magnetic induction component B_x can be calculated as:

$$|B_x(x,y)| = \frac{\hbar}{e \cdot t}\frac{\partial \varphi_{MAG}(x,y)}{\partial y}$$

where $\hbar$ is the reduced Planck constant, e the electron charge and t the total variable thickness along the nanostructure width. Further details on the electron holography experiments and data analysis can be found in the SI and in Refs. 50,53.

ASSOCIATED CONTENT

Supporting Information. Preservation of the nanowires' geometry as a function of the annealing temperature. Normalized net magnetic flux of the nanowires as a function of the annealing temperature.

The following files are available free of charge.

Supp_Inf_Pablo-Navarro et al. 2017.docx

AUTHOR INFORMATION

Corresponding Author:

*César Magén (cmagend@unizar.es)

Instituto de Ciencia de Materiales de Aragón (ICMA)

Universidad de Zaragoza-CSIC

Facultad de Ciencias

Pedro Cerbuna 12. 50009 Zaragoza, Spain.

Tel: +34 876 553354

Fax: +34 976 761229

ACKNOWLEDGEMENT

All authors acknowledge financial support from the Spanish Ministry of Economy and Competitiveness through the projects MAT2014-51982-C2 and MAT2015-69725-REDT, from the COST project CELINA and from the Aragon Regional Government (Construyendo Europa desde Aragón) through the project E26 with European Social Fund funding. J. P.-N. grant is funded by the Ayuda para Contratos Predoctorales para la Formación de Doctores, Convocatoria Res. 05/06/15 (BOE 12/06/15) of the Secretaría de Estado de Investigación, Desarrollo e Innovación in the Subprograma Estatal de Formación of the Spanish Ministry of Economy and Competitiveness with the participation of the European Social Fund.

REFERENCES

(1) van Dorp, W. F.; Hagen, C. W. A Critical Literature Review of Focused Electron Beam Induced Deposition. *J. Appl. Phys.* **2008**, *104*, 81301.

(2) Utke, I.; Hoffmann, P.; Melngailis, J. Gas-Assisted Focused Electron Beam and Ion Beam Processing and Fabrication. *J. Vac. Sci. Technol. B Microelectron. Nanom. Struct.* **2008**, *26*, 1197.

(3) Huth, M.; Porrati, F.; Schwalb, C.; Winhold, M.; Sachser, R.; Dukic, M.; Adams, J.; Fantner, G. Focused Electron Beam Induced Deposition: A Perspective. *Beilstein J. Nanotechnol.* **2012**, *3*, 597–619.

(4) Madsen, D. N.; Mølhave, K.; Mateiu, R.; Rasmussen, A. M.; Brorson, M.; Jacobsen, C. J. H.; Bøggild, P. Soldering of Nanotubes onto Microelectrodes. *Nano Lett.* **2003**, *3*, 47–49.

(5) Riazanova, A. V; Costanzi, B. N.; Aristov, A.; Rikers, Y. G. M.; Ström, V.; Mulders, J. J. L.; Kabashin, A. V; Dahlberg, E. D.; Belova, L. M. Gas-Assisted Electron-Beam-Induced Nanopatterning of High-Quality Si-Based Insulator. *Nanotechnology* **2014**, *25*, 155301.

(6) Utke, I.; Hoffmann, P.; Berger, R.; Scandella, L. High-Resolution Magnetic Co Supertips Grown by a Focused Electron Beam. *Appl. Phys. Lett.* **2002**, *80*, 4792.

(7) Lau, Y. M.; Chee, P. C.; Thong, J. T. L.; Ng, V. Properties and Applications of Cobalt-Based Material Produced by Electron-Beam-Induced Deposition. *J. Vac. Sci. Technol. A Vacuum, Surfaces, Film.* **2002**, *20*, 1295–1302.

(8) Winhold, M.; Weirich, P. M.; Schwalb, C. H.; Huth, M. Superconductivity and Metallic Behavior in Pb X C Y O δ Structures Prepared by Focused Electron

Beam Induced Deposition. *Appl. Phys. Lett.* **2014**, *105*, 162603.

(9) Bøggild, P.; Hansen, T. M.; Tanasa, C.; Grey, F. Fabrication and Actuation of Customized Nanotweezers with a 25 Nm Gap. *Nanotechnology* **2001**, *12*, 331–335.

(10) Utke, I.; Dwir, B.; Leifer, K.; Cicoira, F.; Doppelt, P.; Hoffmann, P.; Kapon, E. Electron Beam Induced Deposition of Metallic Tips and Wires for Microelectronics Applications. *Microelectron. Eng.* **2000**, *53*, 261–264.

(11) Bret, T.; Hofmann, T.; Edinger, K. Industrial Perspective on Focused Electron Beam-Induced Processes. *Appl. Phys. A* **2014**, *117*, 1607–1614.

(12) Shawrav, M. M.; Taus, P.; Wanzenboeck, H. D.; Schinnerl, M.; Stöger-Pollach, M.; Schwarz, S.; Steiger-Thirsfeld, A.; Bertagnolli, E. Highly Conductive and Pure Gold Nanostructures Grown by Electron Beam Induced Deposition. *Sci. Rep.* **2016**, *6*, 34003.

(13) Winkler, R.; Schmidt, F. P.; Haselmann, U.; Fowlkes, J. D.; Lewis, B. B.; Kothleitner, G.; Rack, P. D.; Plank, H. Direct-Write 3D Nanoprinting of Plasmonic Structures. *ACS Appl. Mater. Interfaces* **2017**, *9*, 8233–8240.

(14) Makise, K.; Mitsuishi, K.; Shimojo, M.; Furuya, K. A Nanosized Photodetector Fabricated by Electron-Beam-Induced Deposition. *Nanotechnology* **2009**, *20*, 425305.

(15) Fernández-Pacheco, A.; Serrano-Ramón, L.; Michalik, J. M.; Ibarra, M. R.; De Teresa, J. M.; O'Brien, L.; Petit, D.; Lee, J.; Cowburn, R. P. Three Dimensional Magnetic Nanowires Grown by Focused Electron-Beam Induced Deposition. *Sci. Rep.* **2013**, *3*, 1492.

(16) Gavagnin, M.; Wanzenboeck, H. D.; Wachter, S.; Shawrav, M. M.; Persson, A.; Gunnarsson, K.; Svedlindh, P.; Stöger-Pollach, M.; Bertagnolli, E. Free-Standing Magnetic Nanopillars for 3D Nanomagnet Logic. *ACS Appl. Mater. Interfaces* **2014**, *6*, 20254–20260.

(17) Kolb, F.; Schmoltner, K.; Huth, M.; Hohenau, A.; Krenn, J.; Klug, A.; List, E. J. W.; Plank, H. Variable Tunneling Barriers in FEBID Based PtC Metal-Matrix Nanocomposites as a Transducing Element for Humidity Sensing. *Nanotechnology* **2013**, *24*, 305501.

(18) Serrano-Ramón, L.; Córdoba, R.; Rodríguez, L. A.; Magén, C.; Snoeck, E.; Gatel, C.; Serrano, I.; Ibarra, M. R.; De Teresa, J. M. Ultrasmall Functional Ferromagnetic Nanostructures Grown by Focused Electron-Beam-Induced Deposition. *ACS Nano* **2011**, *5*, 7781–7787.

(19) Vavassori, P.; Pancaldi, M.; Perez-Roldan, M. J.; Chuvilin, A.; Berger, A. Remote Magnetomechanical Nanoactuation. *Small* **2016**, *12*, 1013–1023.

(20) Botman, A.; Mulders, J. J. L.; Hagen, C. W. Creating Pure Nanostructures from Electron-Beam-Induced Deposition Using Purification Techniques: A Technology Perspective. *Nanotechnology* **2009**, *20*, 372001.

(21) Utke, I.; Michler, J.; Gasser, P.; Santschi, C.; Laub, D.; Cantoni, M.; Buffat, P. t. A.; Jiao, C.; Hoffmann, P. Cross Section Investigations of Compositions and Sub-Structures of Tips Obtained by Focused Electron Beam Induced Deposition. *Adv. Eng. Mater.* **2005**, *7*, 323–331.

(22) Lukasczyk, T.; Schirmer, M.; Steinrück, H.-P.; Marbach, H. Electron-Beam-Induced Deposition in Ultrahigh Vacuum: Lithographic Fabrication of Clean Iron Nanostructures. *Small* **2008**, *4*, 841–846.

(23) Bernau, L.; Gabureac, M.; Erni, R.; Utke, I. Tunable Nanosynthesis of Composite Materials by Electron-Impact Reaction. *Angew. Chemie Int. Ed.* **2010**, *49*, 8880–8884.

(24) Winkler, R.; Geier, B.; Plank, H. Spatial Chemistry Evolution during Focused Electron Beam-Induced Deposition: Origins and Workarounds. *Appl. Phys. A* **2014**, *117*, 1675–1688.

(25) De Teresa, J. M.; Córdoba, R.; Fernández-Pacheco, A.; Montero, O.; Strichovanec, P.; Ibarra, M. R. Origin of the Difference in the Resistivity of As-Grown Focused-Ion- and Focused-Electron-Beam-Induced Pt Nanodeposits. *J. Nanomater.* **2009**, *2009*, 1–11.

(26) Córdoba, R.; Sesé, J.; De Teresa, J. M. M.; Ibarra, M. R. R. High-Purity Cobalt Nanostructures Grown by Focused-Electron-Beam-Induced Deposition at Low Current. *Microelectron. Eng.* **2010**, *87*, 1550–1553.

(27) Belova, L. M.; Dahlberg, E. D.; Riazanova, A.; Mulders, J. J. L.; Christophersen, C.; Eckert, J. Rapid Electron Beam Assisted Patterning of Pure Cobalt at Elevated Temperatures via Seeded Growth. *Nanotechnology* **2011**, *22*, 145305.

(28) Mulders, J. J. L.; Belova, L. M.; Riazanova, a. Electron Beam Induced Deposition at Elevated Temperatures: Compositional Changes and Purity Improvement. *Nanotechnology* **2010**, *22*, 55302.

(29) Tanaka, M.; Shimojo, M.; Takeguchi, M.; Mitsuishi, K.; Furuya, K. Formation of Iron Nano-Dot Arrays by Electron Beam-Induced Deposition Using an Ultrahigh Vacuum Transmission Electron Microscope. *J. Cryst. Growth* **2005**, *275*, 2361–2366.

(30) Takeguchi, M.; Shimojo, M.; Furuya, K. Fabrication of Magnetic Nanostructures Using Electron Beam Induced Chemical Vapour Deposition. *Nanotechnology* **2005**, *16*, 1321–1325.

(31) Puydinger dos Santos, M. V.; Velo, M. F.; Domingos, R. D.; Zhang, Y.; Maeder, X.; Guerra-Nuñez, C.; Best, J. P.; Béron, F.; Pirota, K. R.; Moshkalev, S.; Diniz, J. A.; Utke I. Annealing-Based Electrical Tuning of Cobalt–Carbon Deposits Grown by Focused-Electron-Beam-Induced Deposition. *ACS Appl. Mater. Interfaces* **2016**, *8*, 32496–32503.

(32) Frabboni, S.; Gazzadi, G. C.; Felisari, L.; Spessot, A. Fabrication by Electron Beam Induced Deposition and Transmission Electron Microscopic Characterization of Sub-10-Nm Freestanding Pt Nanowires. *Appl. Phys. Lett.* **2006**, *88*, 213116.

(33) Plank, H.; Kothleitner, G.; Hofer, F.; Michelitsch, S. G.; Gspan, C.; Hohenau, A.; Krenn, J. Optimization of Postgrowth Electron-Beam Curing for Focused Electron-Beam-Induced Pt Deposits. *J. Vac. Sci. Technol. B, Nanotechnol. Microelectron. Mater. Process. Meas. Phenom.* **2011**, *29*, 51801.

(34) Plank, H.; Noh, J. H.; Fowlkes, J. D.; Lester, K.; Lewis, B. B.; Rack, P. D. Electron-Beam-Assisted Oxygen Purification at Low Temperatures for Electron-Beam-Induced Pt Deposits: Towards Pure and High-Fidelity Nanostructures. *ACS Appl. Mater. Interfaces* **2014**, *6*, 1018–1024.

(35) Belić, D.; Shawrav, M. M.; Gavagnin, M.; Stöger-Pollach, M.; Wanzenboeck, H. D.; Bertagnolli, E. Direct-Write Deposition and Focused-Electron-Beam-Induced Purification of Gold Nanostructures. *ACS Appl. Mater. Interfaces* **2015**, *7*, 2467–2479.

(36) Roberts, N. A.; Fowlkes, J. D.; Magel, G. A.; Rack, P. D. Enhanced Material Purity and Resolution via Synchronized Laser Assisted Electron Beam Induced Deposition of Platinum. *Nanoscale* **2013**, *5*, 408–415.

(37) Roberts, N. A.; Gonzalez, C. M.; Fowlkes, J. D.; Rack, P. D. Enhanced by-Product Desorption via Laser Assisted Electron Beam Induced Deposition of W(CO)6 with Improved Conductivity and Resolution. *Nanotechnology* **2013**, *24*, 415301.

(38) Gazzadi, G. C.; Frabboni, S. Structural Transitions in Electron Beam Deposited Co-Carbonyl Suspended Nanowires at High Electrical Current Densities. *Beilstein J. Nanotechnol.* **2015**, *6*, 1298–1305.

(39) Shimojo, M.; Takeguchi, M.; Tanaka, M.; Mitsuishi, K.; Furuya, K. Electron Beam-Induced Deposition Using Iron Carbonyl and the Effects of Heat Treatment on Nanostructure. *Appl. Phys. A Mater. Sci. Process.* **2004**, *79*, 1869–1872.

(40) Takeguchi, M.; Shimojo, M.; Furuya, K. Nanostructure Fabrication by Electron-Beam-Induced Deposition with Metal Carbonyl Precursor and Water Vapor. *Jpn. J. Appl. Phys.* **2007**, *46*, 6183–6186.

(41) Henry, M. R.; Kim, S.; Fedorov, A. G. High Purity Tungsten Nanostructures via Focused Electron Beam Induced Deposition with Carrier Gas Assisted Supersonic Jet Delivery of Organometallic Precursors. *J. Phys. Chem. C* **2016**, *120*, 10584–10590.

(42) Mehendale, S.; Mulders, J. J. L.; Trompenaars, P. H. F. A New Sequential EBID Process for the Creation of Pure Pt Structures from MeCpPtMe $_3$. *Nanotechnology* **2013**, *24*, 145303.

(43) Dobrovolskiy, O. V; Kompaniiets, M.; Sachser, R.; Porrati, F.; Gspan, C.; Plank, H.; Huth, M. Tunable Magnetism on the Lateral Mesoscale by Post-Processing of Co/Pt Heterostructures. *Beilstein J. Nanotechnol.* **2015**, *6*, 1082–1090.

(44) Begun, E.; Dobrovolskiy, O. V; Kompaniiets, M.; Sachser, R.; Gspan, C.; Plank, H.; Huth, M. Post-Growth Purification of Co Nanostructures Prepared by Focused Electron Beam Induced Deposition. *Nanotechnology* **2015**, *26*, 75301.

(45) Villamor, E.; Casanova, F.; Trompenaars, P. H. F.; Mulders, J. J. L. Embedded Purification for Electron Beam Induced Pt Deposition Using MeCpPtMe 3. *Nanotechnology* **2015**, *26*, 95303.

(46) Höflich, K.; Yang, R. Bin; Berger, A.; Leuchs, G.; Christiansen, S. The Direct Writing of Plasmonic Gold Nanostructures by Electron-Beam-Induced Deposition. *Adv. Mater.* **2011**, *23*, 2657–2661.

(47) Fernández-Pacheco, A.; De Teresa, J. M.; Córdoba, R.; Ibarra, M. R. Magnetotransport Properties of High-Quality Cobalt Nanowires Grown by Focused-Electron-Beam-Induced Deposition. *J. Phys. D. Appl. Phys.* **2009**, *42*, 55005.

(48) Córdoba, R.; Sharma, N.; Kölling, S.; Koenraad, P. M.; Koopmans, B. High-Purity 3D Nano-Objects Grown by Focused-Electron-Beam Induced Deposition. *Nanotechnology* **2016**, *27*, 355301.

(49) De Teresa, J. M.; Fernández-Pacheco, A.; Córdoba, R.; Serrano-Ramón, L.; Sangiao, S.; Ibarra, M. R. Review of Magnetic Nanostructures Grown by Focused Electron Beam Induced Deposition (FEBID). *J. Phys. D. Appl. Phys.* **2016**, *49*, 243003.

(50) Pablo-Navarro, J.; Sanz-Hernández, D.; Magén, C.; Fernández-Pacheco, A.; de Teresa, J. M. Tuning Shape, Composition and Magnetization of 3D Cobalt Nanowires Grown by Focused Electron Beam Induced Deposition (FEBID). *J. Phys. D. Appl. Phys.* **2017**, *50*, 18LT01.

(51) Nikulina, E.; Idigoras, O.; Porro, J. M.; Vavassori, P.; Chuvilin, A.; Berger, A. Origin and Control of Magnetic Exchange Coupling in between Focused Electron Beam Deposited Cobalt Nanostructures. *Appl. Phys. Lett.* **2013**, *103*, 123112.

(52) Pablo-Navarro, J.; Magén, C.; De Teresa, J. M. Three-Dimensional Core-Shell Ferromagnetic Nanowires Grown by Focused Electron Beam Induced Deposition. *Nanotechnology* **2016**, *27*.

(53) Pablo-Navarro, J.; Magén, C.; de Teresa, J. M. Three-Dimensional Core–shell Ferromagnetic Nanowires Grown by Focused Electron Beam Induced Deposition. *Nanotechnology* **2016**, *27*, 285302.

(54) Earnshaw, A.; Greenwood, N. *Chemistry of the Elements*; 2nd, Ed.; Butterworth-Heinemann, 1997.

(55) Sucksmith, W.; Thompson, J. E. The Magnetic Anisotropy of Cobalt. *Proc. R. Soc. A Math. Phys. Eng. Sci.* **1954**, *225*, 362–375.

GRAPHIC TABLE OF CONTENTS